

On the physical reality of overlooked open clusters

Andrés E. Piatti^{1,2*}

¹*Consejo Nacional de Investigaciones Científicas y Técnicas, Av. Rivadavia 1917, C1033AAJ, Buenos Aires, Argentina*

²*Observatorio Astronómico, Universidad Nacional de Córdoba, Laprida 854, 5000, Córdoba, Argentina*

Accepted XXX. Received YYY; in original form ZZZ

ABSTRACT

We present *UBVRI* and *CT₁T₂* photometry for fifteen catalogued open clusters of relative high brightness and compact appearance. From these unprecedented photometric data sets, covering wavelengths from the blue up to the near-infrared, we performed a thorough assessment of their reality as stellar aggregates. We statistically assigned to each observed star within the object region a probability of being a fiducial feature of that field in terms of its local luminosity function, colour distribution and stellar density. Likewise, we used accurate parallaxes and proper motions measured by the *Gaia* satellite to help our decision on the open cluster reality. Ten catalogued aggregates did not show any hint of being real physical systems; three of them had been assumed to be open clusters in previous studies, though. On the other hand, we estimated reliable fundamental parameters for the remaining five studied objects, which were confirmed as real open clusters. They resulted to be clusters distributed in a wide age range, $8.0 \leq \log(t \text{ yr}^{-1}) \leq 9.4$, of solar metal content and placed between 2.0 and 5.5 kpc from the Sun. Their ages and metallicities are in agreement with the presently known picture of the spatial distribution of open clusters in the Galactic disc.

Key words: techniques: photometric – Galaxy: open clusters and associations: general.

1 INTRODUCTION

According to the most updated version of the open cluster catalogue compiled by Dias et al. (2002, version 3.4 as of 2016 January), a very limited number of objects have been studied with some detail. Indeed, many of the catalogue’s entries correspond to stellar overdensities (e.g. Collinder 1931; Ruprecht 1966) which deserve further analyses in order to confirm their physical nature. Hence, we have recently made use of available multi-band imaging with the aim of improving the statistics of well studied open clusters. We assessed the reality of the observed catalogued objects as real open clusters and, for those confirmed, estimated their structural and fundamental parameters, studied their dynamical evolution, etc (e.g. Piatti 2016).

In this paper we complete the analysis of every open cluster observed through the Johnson *UBV*, Kron-Cousins *RI* and Washington *CT₁T₂* photometric passbands during the observing campaign carried out at the Cerro Tololo Inter-American Observatory (CTIO), Chile, in 2011 January 31–February 4 (CTIO programme #2011A-0114, PI: Clariá). The objects had been originally selected to examine how the abundance gradient in the Galactic disc evolved

in time and along different Galactic longitudes by comparing the abundance gradients corresponding to various groups of open clusters of different ages and positions. The greater the number of open clusters with well determined parameters, the more precise and detailed the analysis of the metal abundance gradient in the Galactic disc as well as its evolution over time.

The present sample comprises unstudied or poorly studied catalogued open clusters that are relatively bright, are composed by a small number of stars and have a relatively compact appearance. In Section 2 we describe the collection and reduction of the available photometric data in order to build extensive and reliable data sets. We carefully evaluated the physical reality of the cluster sample from colour-magnitude and colour-colour diagrams in Section 3, while in Section 4 we estimate the fundamental parameters of the confirmed stellar aggregates and discuss the results. Finally, Section 7 summarizes the main conclusions of this work.

* E-mail: andres@oac.unc.edu.ar

2 DATA COLLECTION AND REDUCTION

The National Optical Astronomy Observatory (NOAO) Science Data Management (SDM) Archives¹ interface were used to download the whole set of publicly available calibration and programme images. The data processing, the calibration to the standard photometric systems and the point spread function photometry for the programme fields were carried out altogether with some previously studied objects, as described in [Piatti et al. \(2017\)](#). We included here two catalogued open clusters (ESO 371-25 and 561-5) for which Washington CT_1 images are publicly available and had not paid particular attention to them until now. The data reduction and photometry for these two objects were performed as described in [Piatti et al. \(2011\)](#). The log of the observations for the presently studied objects with the main astrometric and observational information is summarized in Table 1.

The final information for each cluster field consists of a running number per star, its x and y coordinates, the mean V magnitude, its rms error and the number of measurements, the colours $U - B$, $B - V$, $V - R$, $V - I$ with their respective rms errors and number of measurements, the T_1 magnitude with its error and number of measurements, and the $C - T_1$ and $T_1 - T_2$ colours with their respective rms errors and number of measurements. Table 2 gives this information for Alessi 14. Only a portion of this table is shown here for guidance regarding its form and content. The whole content of Table 2, as well as those for the remaining cluster fields (Tables 3-16), are available in the online version of the journal.

3 COLOUR-MAGNITUDE DIAGRAM ANALYSIS

We based our analysis of the selected objects on their colour-magnitude diagrams (CMDs) and colour-colour (CC) diagrams, once we estimated the open cluster extents, extracted the resulting multi-band photometry for every stars located within the object areas and thoroughly judged their reality as stellar aggregates.

In order to estimate the cluster radii we built stellar density radial profiles from their geometrical centres. Those centres were adopted from single Gaussian fits performed to the stellar density distributions along the x and y directions by using the `NGAUSSFIT` routine in the `STSDAS/IRAF` package. We repeated the fits for projected stellar density distributions built from the number of stars counted within intervals of 20 (5.8), 40 (11.6), 60 (17.4), 80 (23.2) and 100 (29.0) pixel (arcsec) wide, and finally we averaged the five different Gaussian centres resulting a typical standard deviation of ± 50 pixels ($\pm 14.5''$) in all cases.

We traced the radial density profiles from star counts previously performed within boxes of 50 pixels (14.5 arcsec) a side distributed throughout the whole FOV, instead of employing rings around the centre of each cluster. The chosen box size allowed us to sample the stellar spatial distribution statistically. We followed this method since it does not require a complete circle of radius r within the observed

FOV to estimate the mean stellar density at that distance. With a stellar density profile that extends far away from the cluster centre -but not too far so as to risk losing the local field-star signature- it is possible to estimate the background level with high precision, which is particularly useful when dealing with clusters composed by a small number of stars. The number of stars per unit area at a given radius r was calculated through the expression:

$$(n_{r+25} - n_{r-25}) / (m_{r+25} - m_{r-25}), \quad (1)$$

where n_r and m_r represent the number of stars and boxes, respectively, included in a circle of radius r . The resulting density profiles expressed as number of stars per arcsec² are shown in Fig. 1. In the figure, we represent the constructed and background subtracted density profiles with open and filled circles, respectively. The average and corresponding rms error of the background level at any distance to the cluster centres were counted by using every available star count measurement at that distance. Then, the mean background and its error was calculated by averaging all these latter values, and indicated by solid and dotted horizontal lines in the figure. The errorbars of the background subtracted density profiles include the mean error of the background level.

As for the cluster radius, we considered here the distance from the cluster centre where the combined cluster plus background stellar density profile is no longer readily distinguished from the background, as is shown in Fig. 1, where we represent the mean radius and its error with vertical solid and dotted lines, respectively. As can be seen, the background level amounts in average to 25 ± 15 per cent of the central stellar density, which suggests that the selected objects can be relatively easily distinguished from the composite field population. In addition, they appear in the sky as relatively small concentrations of stars, in average, of 1.6 ± 0.7 arcmin in radius.

We built six CMDs and three CCDs diagrams by extracting every star from our $UBVRI - CT_1T_2$ photometric data sets located within the cluster radii estimated above. We then cleaned them from the field star contamination by applied a statistical method which accounts for the luminosity function, colour distribution and stellar density of the stars distributed along the cluster line of sight.

The procedure was developed by [Piatti & Bica \(2012\)](#), see their Fig. 12) and successfully used elsewhere (e.g. [Piatti 2014](#); [Piatti et al. 2015a,b](#); [Piatti & Bastian 2016](#), and references therein). Briefly, it compares a extracted cluster CMD to different field-star CMDs composed of stars located reasonably far from the object, but not too far so as to risk losing the local field-star signature in terms of stellar density, luminosity function and/or colour distribution. The comparison between field-star and cluster CMDs is carried out by using boxes which vary their sizes from one place to another throughout the CMD and are centred on the positions of every star found in the field-star CMD. Note that it uses the same boxes in both cluster and field-star CMDs, and that the comparison is performed for each individual box. Here we chose four field regions, each one designed to cover an equal area as that of the cluster, and placed around the cluster. Hence, we obtained four distinct cleaned cluster CMDs.

When comparing the four cleaned CMDs, we counted

¹ <http://www.noao.edu/sdm/archives.php>.

Table 1. Observations log of selected star clusters.

Cluster	R.A. (h m s)	Dec. (° ' ")	l (°)	b (°)	filter	exposure (sec)	airmass
Alessi 14	6 30 25.9	+09 44 28	201.8790	-0.1796	<i>U</i>	90, 480	1.35, 1.35
					<i>B</i>	60, 300	1.32, 1.32
					<i>V</i>	40, 180	1.31, 1.31
					<i>R</i>	20, 120	1.31, 1.31
					<i>I</i>	10, 90	1.30, 1.30
					<i>C</i>	90, 420	1.33, 1.33
ESO 211-9	9 16 44.2	-50 16 59	271.9430	-0.7949	<i>U</i>	150, 600	1.07, 1.07
					<i>B</i>	100, 400	1.09, 1.09
					<i>V</i>	90, 200	1.10, 1.10
					<i>R</i>	30, 140	1.11, 1.11
					<i>I</i>	20, 120	1.12, 1.12
					<i>C</i>	120, 580	1.08, 1.08
ESO 260-6	8 46 17.3	-47 41 06	266.6933	-2.8282	<i>U</i>	60, 480	1.06, 1.06
					<i>B</i>	60, 120	1.05, 1.05
					<i>V</i>	20, 60, 180	1.05, 1.05, 1.05
					<i>R</i>	20, 120	1.05, 1.05
					<i>I</i>	10, 90	1.05, 1.05
					<i>C</i>	50, 420	1.05, 1.05
ESO 315-14	9 35 25.1	-39 32 03	266.7956	9.2082	<i>U</i>	90, 480	1.04, 1.04
					<i>B</i>	60, 320	1.07, 1.07
					<i>V</i>	60, 180	1.09, 1.10
					<i>R</i>	30, 120	1.11, 1.11
					<i>I</i>	15, 90	1.12, 1.12
					<i>C</i>	80, 400	1.05, 1.06
ESO 371-25	8 53 00.0	-35 28 01	258.0026	5.8612	<i>C</i>	300, 300	1.01, 1.01
					<i>R</i>	10, 10, 30, 30	1.01, 1.01, 1.01, 1.01
ESO 383-10	13 31 30.0	-35 03 56	312.1324	27.0895	<i>U</i>	15, 180	1.02, 1.02
					<i>B</i>	10, 120	1.01, 1.01
					<i>V</i>	7, 80	1.01, 1.01
					<i>R</i>	5, 60	1.01, 1.01
					<i>I</i>	4, 60	1.01, 1.01
					<i>C</i>	15, 180	1.02, 1.02
ESO 430-9	8 02 24.0	-29 46 01	247.1599	0.5167	<i>U</i>	90, 450	1.00, 1.00
					<i>B</i>	60, 200	1.02, 1.01
					<i>V</i>	60, 200	1.02, 1.02
					<i>R</i>	15, 120	1.03, 1.03
					<i>I</i>	10, 10, 90	1.04, 1.04, 1.03
					<i>C</i>	80, 400	1.01, 1.01
ESO 437-61	10 48 03.0	-29 23 30	273.0624	26.2286	<i>U</i>	90, 400	1.07, 1.07
					<i>B</i>	60, 300	1.04, 1.04
					<i>V</i>	40, 200	1.03, 1.03
					<i>R</i>	20, 120	1.02, 1.03
					<i>I</i>	10, 90	1.02, 1.02, 1.02
					<i>C</i>	80, 360	1.05, 1.06
ESO 493-3	7 39 42.0	-27 17 00	242.4794	-2.5035	<i>U</i>	60, 240	1.08, 1.09
					<i>B</i>	20, 150	1.06, 1.06
					<i>V</i>	10, 120	1.05, 1.05
					<i>R</i>	10, 90	1.03, 1.04
					<i>I</i>	10, 60	1.03, 1.03
					<i>C</i>	60, 180	1.07, 1.07
ESO 561-5	7 59 18.0	-22 41 00	240.7668	+3.6558	<i>C</i>	300	1.08
					<i>R</i>	30	1.08

Table 1. continued.

Cluster	R.A. (h m s)	Dec. (° ' ")	l (°)	b (°)	filter	exposure (sec)	airmass
Hogg 9	10 58 24.5	-59 03 11	288.8399	+0.6910	<i>U</i>	80, 480	1.16, 1.17
					<i>B</i>	60, 300	1.19, 1.19
					<i>V</i>	40, 180	1.20, 1.20
					<i>R</i>	10, 20, 100	1.22, 1.21, 1.21
					<i>I</i>	10, 80	1.22, 1.20
					<i>C</i>	70, 420	1.18, 1.18
Miller 1	9 25 40.8	-53 13 30	275.0021	-1.8977	<i>U</i>	90, 500	1.09, 1.09
					<i>B</i>	80, 320	1.08, 1.09
					<i>V</i>	60, 180	1.09, 1.09
					<i>R</i>	20, 120	1.10, 1.10
					<i>I</i>	15, 90	1.10, 1.10
					<i>C</i>	90, 420	1.09, 1.09
NGC 5269	13 44 44.0	-62 54 54	308.9554	-0.6682	<i>U</i>	90, 540	1.21, 1.21
					<i>B</i>	80, 80, 300	1.22, 1.22, 1.21
					<i>V</i>	60, 200	1.22, 1.22
					<i>R</i>	15, 120	1.23, 1.22
					<i>I</i>	15, 90	1.23, 1.23
					<i>C</i>	80, 420	1.21, 1.20
Ruprecht 5	6 55 14.2	-18 36 00	230.0043	-7.5541	<i>U</i>	80, 540	1.05, 1.05
					<i>B</i>	60, 360	1.09, 1.08
					<i>V</i>	60, 220	1.11, 1.11
					<i>R</i>	50, 140	1.11, 1.11
					<i>I</i>	10, 20, 100	1.13, 1.12, 1.12
					<i>C</i>	80, 480	1.07, 1.07
Ruprecht 15	7 19 31.7	-19 37 48	233.5384	-2.9061	<i>U</i>	90, 480	1.02, 1.02
					<i>B</i>	60, 240	1.04, 1.04
					<i>V</i>	40, 150	1.05, 1.05
					<i>R</i>	20, 100	1.05, 1.06
					<i>I</i>	10, 80	1.06, 1.06
					<i>C</i>	80, 420	1.03, 1.03

the number of times a star remained unsubtracted in all of them. Thus, we distinguished stars that appear once, twice, until four times, respectively. Stars appearing once can be associated to a probability $P \leq 25\%$ of being a fiducial feature in the cleaned CMD, i.e., stars that could most frequently be found in a field-star CMD. Stars that appear twice ($P = 50\%$) could equally likely be associated with either the field or the object of interest; and those with $P \geq 75\%$, i.e., stars found in three or four cleaned CMDs, belong predominantly to the cleaned CMD rather than to the field-star CMDs. Note that the latter can be cluster stars, or a group of stars that are distinguishable in terms of luminosity function, colour distribution and stellar density without forming a physical system. Nevertheless, the cleaning of the cluster CMDs is a mandatory step in order to assess the real status of a catalogued aggregate and, if confirmed as a star cluster, to estimate its astrophysical properties. Statistically speaking, a certain amount of residuals is expected, which depends on the degree of variability of the stellar density, luminosity function and colour distribution of the star fields.

Figures 2 to 16 show the whole set of CMDs and CC diagrams for the cluster sample that can be exploited from the present extensive multi-band photometry. They include

every magnitude and colour measurements of stars located within the respective cluster radii. We have also incorporated to the figures the statistical probabilities P obtained above by distinguishing stars with different colour symbols as follows: stars that statistically belong to the field ($P \leq 25\%$, pink), stars that might belong to either the field or the cluster ($P = 50\%$, light blue), and stars that predominantly populate the cluster region ($P \geq 75\%$, dark blue).

3.1 Assessment on the physical reality

The basic challenge of trying to confirm the physical reality of the studied catalogued open clusters was conducted as follows: i) Identify a spatial overdensity relative to the background distribution (see Section 3, Fig. 1); ii) Select stars with parallaxes (π) and proper motions (μRA , μDEC) measured by the *Gaia* satellite (Gaia Collaboration et al. 2016). Here we decided to dodge the UCAC4 (Zacharias et al. 2013) catalogue, simply because its mean proper motion errors are $\sim 4 \text{ mas yr}^{-1}$, which are largely surpassed by those obtained by the *Gaia* mission ($\sim 1 \text{ mas yr}^{-1}$). Note that proper motions distribution observed in an open cluster is mainly dominated by the observational errors (Dias et al.

Table 2. *UBVRI* and *CT₁T₂* data of stars in the field of Alessi 14.

Star	<i>x</i> (pixel)	<i>y</i> (pixel)	<i>V</i> (mag)	<i>U</i> − <i>B</i> (mag)	<i>B</i> − <i>V</i> (mag)	<i>V</i> − <i>R</i> (mag)	<i>V</i> − <i>I</i> (mag)	<i>T</i> ₁ (mag)	<i>C</i> − <i>T</i> ₁ (mag)	<i>T</i> ₁ − <i>T</i> ₂ (mag)
752	136.390	4032.939	12.932 0.010 2	1.280 0.035 2	2.244 0.018 2	-0.353 0.001 2	0.360 0.010 2	13.163 0.015 2	3.044 0.002 2	0.830 0.010 2
753	2568.867	4033.493	12.888 0.014 2	0.266 0.006 1	1.323 0.005 1	-0.802 0.001 2	-0.490 0.010 2	13.566 0.020 2	1.125 0.003 2	0.423 0.012 2
754	707.266	4034.801	13.801 0.007 2	0.257 0.027 2	1.615 0.020 2	-0.673 0.001 2	-0.230 0.001 2	14.350 0.011 2	1.683 0.013 2	0.556 0.001 2

Columns list a running number per star, its *x* and *y* coordinates, the mean *V* magnitude, its rms error and the number of measurements, the colours *U* − *B*, *B* − *V*, *V* − *R*, *V* − *I* with their respective rms errors and number of measurements, the *T*₁ magnitude with its error and number of measurements, and the *C* − *T*₁ and *T*₁ − *T*₂ colours with their respective rms errors and number of measurements.

2014; Sampedro & Alfaro 2016). iii) Test whether potential members, defined as those stars which comply with:

$$|\pi_j - \pi_k| \leq |\sigma(\pi_j) + \sigma(\pi_k)|, \quad (2)$$

$$|\mu RA_j - \mu RA_k| \leq |\sigma(\mu RA_j) + \sigma(\mu RA_k)|, \quad (3)$$

$$|\mu DEC_j - \mu DEC_k| \leq |\sigma(\mu DEC_j) + \sigma(\mu DEC_k)|, \quad (4)$$

where *j* and *k* refer to the *j*-th and *k*-th star, have positions in the CMDs and CC diagrams consistent with an age, distance and metallicity within the photometric uncertainties (isochrone fitting). This last step also includes considering the probabilities *P* estimated in Section 3.

We searched for parallaxes and proper motions around the central coordinates of the studied objects and within their estimated radii using the *Gaia* DR1 release (Gaia Collaboration et al. 2016). The results are shown in Table 17, where each star is identified by a running number. We employed the same numbering to place these stars in the CMDs and CC diagrams (Figs. 2 to 16) of those objects with available information from *Gaia*. We transformed the parallaxes to true distance moduli using the expression $(m - M)_o = 5 \times \log(100/\pi)$.

Only ESO 430-9 and NGC 5269 contain stars with *P* ≥ 75% and parallaxes in very good agreement with the derived true distance moduli (see Section 4). As can be seen in Figs. 8 and 14, both clusters have other relatively bright stars (*V* ≤ 14.0 mag) -those supposed to mainly form the stellar aggregates- with a high probability of being cluster stars (*P* ≥ 75%) that are pretty well matched by the same isochrone within the observable dispersion. In the case of ESO 315-14 (Fig. 5), ESO 383-10 (Fig. 7) and ESO 493-3 (Fig. 10), the bright stars' parallaxes and proper motions do not allow us to draw positive conclusions on the cluster reality, in good agreement with the resulting photometric probabilities (*P* ≤ 50%, except for ESO 315-14). Finally, the resulting distance moduli obtained for one bright star in the field of ESO 260-6 (Fig. 4), Hogg 9 (Fig. 12) and Ruprecht 15 (Fig. 16), respectively, suggest that they are foreground stars. Additionally, since the CMDs and CC diagrams do not show any hint for a cluster sequence (stars with *P* ≥ 75%), we discard these objects as real open clusters.

For catalogued clusters without *Gaia* outcomes, we had to rely our analysis on the photometric probabilities obtained in Section 3. Fortunately, ESO 371-25 (Fig. 6) and ESO 561-5 (Fig. 11) -with only *CT*₁ photometry- turned out to be clear open clusters. The latter contains only main sequence turnoff (MSTO) and red clump stars, a signature of an advanced dynamical stage (see Piatti et al. 2017); stars

fainter than *T*₁ ∼ 16.0 mag with *P* ≥ 75% (blue filled circles) are residuals from the cleaning procedure. ESO 211-6 (Fig. 3) also shows an evident star cluster sequence. This is not the case of Alessi 14 (Fig. 2), ESO 437-61 (Fig. 9), Miller 1 (Fig. 13) and Ruprecht 5 (Fig. 15). Their CMDs and CC diagrams (stars with *P* ≥ 75%) do not simultaneously exhibit star sequences typical of star clusters. We recall that these objects were catalogued as open clusters because of the concentration in the sky of a small number of relatively bright stars, so that those stars should mainly define the main cluster features in the CMDs and CC diagrams.

Three of the ten resulting non-physical systems, namely, ESO 383-10, ESO 437-61 and Hogg 9 have some previous relatively relevant studies. Pavani & Bica (2007) concluded from 2MASS photometry and UCAC2 (Zacharias et al. 2004) proper motions that ESO 383-10 is an open cluster remnant. However, the *J* vs. *J* − *H* CMD has a very narrow baseline, making field stars appear following a sequence similar to that of an open cluster. Such a star sequence is also seen in Fig. 7 -less clear in panels involving the *UB* passbands-; it does not resemble that of a star cluster of 2 Gyr located at 1.0 kpc from the Sun, as derived by the authors. Moreover, the parallax of star #2 converts to a heliocentric distance of ∼ 0.3 kpc. The UCAC2 proper motion uncertainties could additionally misled the analysis. ESO 437-61 resulted to be an open cluster in its late stage of dynamical evolution, according to a star count analysis by Bica et al. (2001). Later, Carraro et al. (2005) concluded that the object is not a physical system from the SPM3 catalogue of proper motions (Girard et al. 2004). Similarly, Moffat & Vogt (1975) had suggested that Hogg 9 could not be a real open cluster, although Ahumada et al. (2007) assumed it as a star cluster and estimated for it an age of 300 Myr from integrated spectroscopy.

4 CLUSTER FUNDAMENTAL PARAMETERS

We derived reliable ages, reddenings and distances of ESO 211-9, ESO 430-9 and NGC 5269 by making use of the six CMDs and three different CC diagrams covering wavelengths from the blue up to the near-infrared (Fig. 3, 8 and 14, respectively). We matched theoretical isochrones computed by Bressan et al. (2012) to the various CMDs and CC diagrams, simultaneously.

As a starting point we took advantage of the shape of the main sequences (MS), its curvature (less and more pronounced), the relative distance between the giant stars and the MSTOs in magnitude and colour separately, among others, to find the age of the isochrone which best matches the cluster's features in the CMDs and CC diagrams, regardless the cluster reddening and distance. From our best choice, we

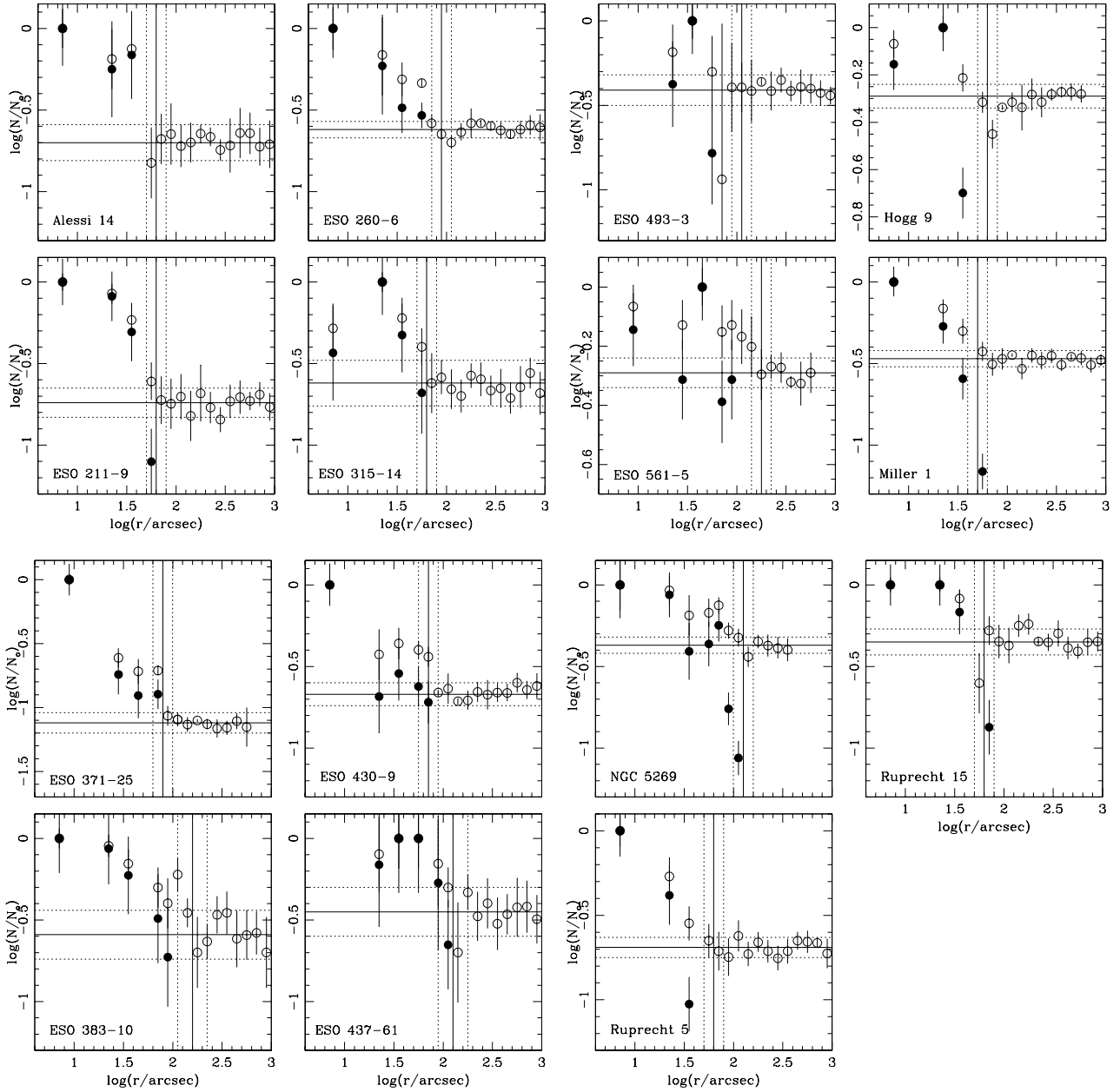


Figure 1. Stellar density profiles normalized to the central density N_0 obtained from star counts. Open and filled circles refer to measured and background subtracted density profiles, respectively.

derived the cluster reddenings by shifting that isochrone in the three CC diagrams following the reddening vectors until their bluest points coincided with the observed ones. Note that this requirement allowed us to use the $V - R$ vs $R - I$ CC diagram as well, even though the reddening vector runs almost parallel to the cluster sequence. In order to enter the isochrones into the CMDs and CC diagrams we used the following ratios: $E(U - B)/E(B - V) = 0.72 + 0.05 \times E(B - V)$ (Hiltner & Johnson 1956); $E(V - R)/E(B - V) = 0.65$, $E(V - I)/E(B - V) = 1.25$, $A_V/E(B - V) = 3.1$ (Cardelli et al. 1989); $E(C - T_1)/E(B - V) = 1.97$, $E(T_1 - T_2)/E(B - V) = 0.692$, $A_{T_1}/E(B - V) = 2.62$ (Geisler 1996). Finally, the adopted $E(B - V)$ colour excesses were used to properly shift the chosen isochrone in the CMDs in order to derive

the cluster true distance moduli $(m - M)_0$ by shifting the isochrone along the magnitude axes. We used isochrones of solar metal content ($[\text{Fe}/\text{H}] = 0.0$ dex) and checked that those for $[\text{Fe}/\text{H}] = \pm 0.2$ dex did not produce any visible difference in the CMDs and CC diagrams. Lower metallicities values ($-0.7 \leq [\text{Fe}/\text{H}] \leq -0.2$, (Paunzen et al. 2010; Heiter et al. 2014)) did not match the CMDs and CC diagrams satisfactorily.

For ESO 371-25 and ESO 561-5 -with only CT_1 photometry- we made use of the age-metallicity diagnostic diagram, δT_1 versus $\delta C - \delta T_1$, which has shown the ability of unambiguously providing age and metallicity estimates, simultaneously (Piatti & Perren 2015, see their Fig. 4). δC and δT_1 are the respective magnitude differences between

Table 17. *Gaia* DR1 parallaxes and proper motions for stars around the studied cluster fields.

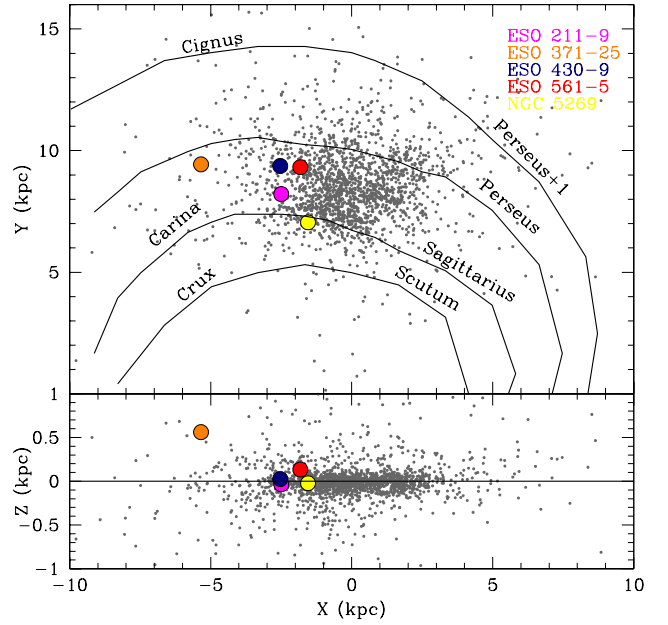
	ID	π (mas)	μ_{RA} (mas yr ⁻¹)	μ_{DEC} (mas yr ⁻¹)
ESO 260-6	1	1.85±0.51	7.06±2.23	-19.89±1.30
ESO 315-14	1	2.27±0.68	-12.05±1.33	-1.08±2.19
	2	0.83±0.33	-6.59±0.99	3.19±1.07
	3	2.06±0.34	-8.28±0.99	-3.59±1.03
ESO 383-10	1	2.33±0.54	-19.97±2.01	-25.08±0.68
	2	3.46±0.54	3.79±1.50	-6.63±0.44
ESO 430-9	1	0.51±0.26	-2.45±0.71	2.17±0.73
ESO 493-3	1	0.78±0.32	-3.45±0.97	1.09±1.17
	2	-0.14±0.92	-2.90±2.55	1.56±2.81
	3	2.54±0.26	-1.48±0.91	32.27±1.05
	4	0.62±0.30	-3.86±0.91	3.00±1.13
	5	1.95±0.29	-14.96±0.91	-0.66±1.07
	6	1.62±0.26	3.40±0.78	-9.54±0.96
	7	2.89±0.33	-10.81±0.97	20.59±1.02
Hogg 9	1	1.23±0.44	-4.50±1.98	1.83±0.93
NGC 5269	1	0.37±0.29	-4.58±0.80	-1.79±0.68
	2	0.31±0.27	-4.75±0.72	-2.04±0.61
	3	0.51±0.24	-4.44±0.63	-2.44±0.55
	4	0.39±0.25	-4.83±0.66	-2.26±0.57
Ruprecht 15	1	0.25±0.47	-2.02±1.07	0.18±1.02

the giant red clump (RC) and the MSTO. The diagnostic diagram allows to derive ages from 1 up to 13 Gyr and metallicities $[\text{Fe}/\text{H}]$ from -2.0 up to +0.5 dex, and is independent of the cluster reddening and distance modulus. We measured C and T_1 magnitudes at the MSTO and RC, then computed δC and δT_1 and entered into Figure 4 of [Piatto & Perren \(2015\)](#) to estimate cluster ages and metallicities (both clusters are of solar metal content within $\sigma[\text{Fe}/\text{H}] = 0.15$ dex). Then, we derived the cluster reddening and distance moduli by matching the respective isochrones to the cluster CMDs. The adopted best matched isochrones for ESO 211-9, ESO 371-25, ESO 430-9, ESO 561-5 and NGC 5269 are overplotted with black solid lines on Fig. 3, 6, 8, 11 and 14, respectively, while the resulting values with their errors for the cluster reddenings, distances, ages are listed in Table 18.

Fig. 17 depicts the spatial distribution of the studied clusters, where we added for comparison purposes the 2167 open clusters catalogued by [Dias et al. \(2002, version 3.4 as of January 2016\)](#) and the schematic positions of the spiral arms ([Drimmel & Spergel 2001; Moitinho et al. 2006](#)). The cluster Galactic coordinates were computed using the derived cluster heliocentric distances, their angular Galactic coordinates and a Galactocentric distance of the Sun of $R_{GC\odot} = 8.3$ kpc ([Hou & Han 2014](#), and references therein). The clusters are distributed outside the circle around the Sun ($d \sim 2.0$ kpc) where the catalogued clusters are mostly concentrated. They belong to the thin Galactic disc, with the exception of ESO 371-25 which is nearly 0.5 kpc above the Galactic plane. The relationship between their positions in the Galaxy and their ages are in agreement with the over-

Table 18. Derived properties of selected open clusters.

Star cluster	$E(B - V)$ (mag)	$(m - M)_o$ (mag)	d (kpc)	$\log(t)$
ESO 211-9	1.40±0.10	12.0±0.3	2.50±0.35	8.70±0.10
ESO 371-25	0.40±0.05	13.7±0.2	5.49±1.25	9.40±0.05
ESO 430-9	0.45±0.05	12.2±0.3	2.75±0.38	8.00±0.10
ESO 561-5	0.25±0.05	11.6±0.2	2.09±0.19	8.90±0.05
NGC 5269	0.25±0.05	11.5±0.3	1.99±0.27	8.50±0.10

**Figure 17.** Galactic spatial distribution of the studied clusters. Open clusters from the catalogue of [Dias et al. \(2002, version 3.4 as of January 2016\)](#) are drawn with gray dots, while the schematic positions of spiral arms ([Drimmel & Spergel 2001; Moitinho et al. 2006](#)) are traced with black solid lines.

all feature of the Galactic disc attained from open cluster statistical analyses (see, e.g. [Bonatto et al. 2006; Joshi et al. 2016](#)).

5 CONCLUSIONS

With the aim of improving the statistics of well studied open clusters, we present a multi-band photometric analysis of 15 catalogued open clusters. The selected sample was chosen on the basis of the relative high brightness and compact appearance of the candidates and because they had not been studied or poorly studied at the time of designing the observational campaign.

We used publicly available Johnson *UBV*, Kron-Cousins *RI* and Washington *C* images obtained at CTIO to produce photometric data sets from which we built six CMDs and three different CC diagrams per object covering wavelengths from the blue up to the near-infrared. This unprecedented multi-band coverage allowed us to thoroughly judged their reality as stellar aggregates.

In order to reliably assess on their physical nature we statistically assigned to each observed star in a given field a probability of being a fiducial feature of that field in terms of its local luminosity function, colour distribution and stellar density. This was accomplished by using a powerful technique that makes use of cells varying in position and size in the CMDs to disentangle the fiducial from the contaminating field stars. To that purpose we first traced the cluster stellar radial profiles and estimated their radii that were used to delimit the region to examine. Likewise, we took advantage of accurate parallaxes and proper motions measured by the *Gaia* satellite to help our decision on the open cluster reality.

Contrarily to what could be expected, as judged from the objects' brightness and compactness, 10 catalogued aggregates did not show any hint of being real physical systems. Three of them (ESO 383-10, ESO 437-61 and Hogg 9) had been treated as open clusters in previous photometric studies. Thus, this result points to the need of a thorough examination of any group of stars believed to be a physical entity by its only appearance in the sky. On the other hand, we estimated reliable fundamental parameters for the remaining 5 studied objects, which were confirmed as real open clusters. By exploiting the wealth of photometric data sets in combination with theoretical isochrones, we found out that the clusters in our sample are in wide age range, $8.0 \leq \log(t \text{ yr}^{-1}) \leq 9.4$, of solar metal content and placed between 2.0 and 5.5 kpc from the Sun. They resulting astrophysical properties are in agreement with the updated known picture of the spatial distribution of ages/metallicities of open clusters in the Galactic disc.

ACKNOWLEDGEMENTS

This work has made use of data from the European Space Agency (ESA) mission *Gaia* (<http://www.cosmos.esa.int/gaia>), processed by the *Gaia* Data Processing and Analysis Consortium (DPAC, <http://www.cosmos.esa.int/web/gaia/dpac/consortium>). Funding for the DPAC has been provided by national institutions, in particular the institutions participating in the *Gaia* Multilateral Agreement. We thank the anonymous referee whose thorough comments and suggestions allowed us to improve the manuscript.

REFERENCES

- Ahumada A. V., Clariá J. J., Bica E., 2007, *A&A*, 473, 437
- Bica E., Santiago B. X., Dutra C. M., Dottori H., de Oliveira M. R., Pavani D., 2001, *A&A*, 366, 827
- Bonatto C., Kerber L. O., Bica E., Santiago B. X., 2006, *A&A*, 446, 121
- Bressan A., Marigo P., Girardi L., Salasnich B., Dal Cero C., Rubele S., Nanni A., 2012, *MNRAS*, 427, 127
- Cardelli J. A., Clayton G. C., Mathis J. S., 1989, *ApJ*, 345, 245
- Carraro G., Dinescu D. I., Girard T. M., van Altena W. F., 2005, *A&A*, 433, 143
- Collinder P., 1931, *Annals of the Observatory of Lund*, 2, B1
- Dias W. S., Alessi B. S., Moitinho A., Lépine J. R. D., 2002, *A&A*, 389, 871
- Dias W. S., Monteiro H., Caetano T. C., Lépine J. R. D., Assafin M., Oliveira A. F., 2014, *A&A*, 564, A79
- Drimmel R., Spergel D. N., 2001, *ApJ*, 556, 181
- Gaia Collaboration Brown A. G. A., Vallenari A., Prusti T., de Bruijne J., Mignard F., Drimmel R., co-authors., 2016, preprint, ([arXiv:1609.04172](https://arxiv.org/abs/1609.04172))
- Geisler D., 1996, *AJ*, 111, 480
- Girard T. M., Dinescu D. I., van Altena W. F., Platais I., Lopez C. E., Monet D. G., 2004, in Clemens D., Shah R., Brainerd T., eds, *Astronomical Society of the Pacific Conference Series* Vol. 317, *Milky Way Surveys: The Structure and Evolution of our Galaxy*. p. 206
- Heiter U., Soubiran C., Netopil M., Paunzen E., 2014, *A&A*, 561, A93
- Hiltner W. A., Johnson H. L., 1956, *ApJ*, 124, 367
- Hou L. G., Han J. L., 2014, *A&A*, 569, A125
- Joshi Y. C., Dambis A., Pandey A. K., Joshi S., 2016, preprint, ([arXiv:1606.06425](https://arxiv.org/abs/1606.06425))
- Moffat A. F. J., Vogt N., 1975, *A&AS*, 20, 125
- Moitinho A., Vázquez R. A., Carraro G., Baume G., Giorgi E. E., Lyra W., 2006, *MNRAS*, 368, L77
- Paunzen E., Heiter U., Netopil M., Soubiran C., 2010, *A&A*, 517, A32
- Pavani D. B., Bica E., 2007, *A&A*, 468, 139
- Piatti A. E., 2014, *MNRAS*, 440, 3091
- Piatti A. E., 2016, *MNRAS*, 463, 3476
- Piatti A. E., Bastian N., 2016, *A&A*, 590, A50
- Piatti A. E., Bica E., 2012, *MNRAS*, 425, 3085
- Piatti A. E., Perren G. I., 2015, *MNRAS*, 450, 3771
- Piatti A. E., Clariá J. J., Parisi M. C., Ahumada A. V., 2011, *PASP*, 123, 519
- Piatti A. E., de Grijs R., Rubele S., Cioni M.-R. L., Ripepi V., Kerber L., 2015a, *MNRAS*, 450, 552
- Piatti A. E., et al., 2015b, *MNRAS*, 454, 839
- Piatti A. E., Dias W. S., Sampedro L. M., 2017, *MNRAS*, in press
- Ruprecht J., 1966, *Bulletin of the Astronomical Institutes of Czechoslovakia*, 17, 33
- Sampedro L., Alfaro E. J., 2016, *MNRAS*, 457, 3949
- Zacharias N., Urban S. E., Zacharias M. I., Wycoff G. L., Hall D. M., Monet D. G., Rafferty T. J., 2004, *AJ*, 127, 3043
- Zacharias N., Finch C. T., Girard T. M., Henden A., Bartlett J. L., Monet D. G., Zacharias M. I., 2013, *AJ*, 145, 44

Figure 2. CMDs and CC diagrams for stars measured in the field of Alessi 14. Colour-scaled symbols represent stars with photometric memberships $P \leq 25\%$ (pink), equals to 50% (light blue) and $\geq 75\%$ (dark blue), respectively.

Figure 3. CMDs and CC diagrams for stars measured in the field of ESO 211-6. Symbols are as in Fig. 2. We overplotted the isochrone which best matches the cluster features (black solid line). In panels involving $U - B$ colours, the isochrone was drawn for complete purposes.

Figure 4. CMDs and CC diagrams for stars measured in the field of ESO 260-6. Symbols are as in Fig. 2. Star with *Gaia* parallax and proper motions is numbered #1 . (see text for details).

Figure 5. CMDs and CC diagrams for stars measured in the field of ESO 315-14. Symbols are as in Fig. 2. Stars with *Gaia* parallaxes and proper motions are numbered from #1 to 3. (see text for details).

Figure 6. CMD for stars measured in the field of ESO 371-25. Symbols are as in Fig. 2. We overplotted the isochrone which best matches the cluster features (black solid line).

Figure 7. CMDs and CC diagrams for stars measured in the field of ESO 383-10. Symbols are as in Fig. 2. Stars with *Gaia* parallaxes and proper motions are numbered from #1 to 2. (see text for details).

Figure 8. CMDs and CC diagrams for stars measured in the field of ESO 430-9. Symbols are as in Fig. 2. Star with *Gaia* parallax and proper motions is numbered #1 (see text for details). We overplotted the isochrone which best matches the cluster features (black solid line).

Figure 9. CMDs and CC diagrams for stars measured in the field of ESO 437-61. Symbols are as in Fig. 2.

Figure 10. CMDs and CC diagrams for stars measured in the field of ESO 493-3. Symbols are as in Fig. 2. Stars with *Gaia* parallaxes and proper motions are numbered from #1 to 7. (see text for details).

Figure 11. CMD for stars measured in the field of ESO 561-5. Symbols are as in Fig. 2. We overplotted the isochrone which best matches the cluster features (black solid line).

Figure 12. CMDs and CC diagrams for stars measured in the field of Hogg9. Symbols are as in Fig. 2. Star with *Gaia* parallax and proper motions is numbered #1. (see text for details).

Figure 13. CMDs and CC diagrams for stars measured in the field of Miller 1. Symbols are as in Fig. 2.

Figure 14. CMDs and CC diagrams for stars measured in the field of NGC 5269. Symbols are as in Fig. 2. Stars with *Gaia* parallaxes and proper motions are numbered from #1 to 4 (see text for details). We overplotted the isochrone which best matches the cluster features (black solid line).

Figure 15. CMDs and CC diagrams for stars measured in the field of Ruprecht 5. Symbols are as in Fig. 2.

Figure 16. CMDs and CC diagrams for stars measured in the field of Ruprecht 15. Symbols are as in Fig. 2. Stars with *Gaia* parallaxes and proper motions is numbered #1. (see text for details).

This paper has been typeset from a $\text{\TeX}/\text{\LaTeX}$ file prepared by the author.